Statistical comparison of InSAR tropospheric correction techniques

CrossMark

D.P.S. Bekaert [a,b,*], R.J. Walters [a], T.J. Wright [a], A.J. Hooper [a], D.J. Parker [b]

[a] COMET, School of Earth and Environment, University of Leeds, United Kingdom
[b] ICAS, School of Earth and Environment, University of Leeds, United Kingdom

ARTICLE INFO

ABSTRACT

Correcting for tropospheric delays is one of the largest challenges facing the interferometric synthetic aperture radar (InSAR) community. Spatial and temporal variations in temperature, pressure, and relative humidity create tropospheric signals in InSAR data, masking smaller surface displacements due to tectonic or volcanic deformation. Correction methods using weather model data, GNSS and/or spectrometer data have been applied in the past, but are often limited by the spatial and temporal resolution of the auxiliary data. Alternatively a correction can be estimated from the interferometric phase by assuming a linear or a power-law relationship between the phase and topography. Typically the challenge lies in separating deformation from tropospheric phase signals. In this study we performed a statistical comparison of the state-of-the-art tropospheric corrections estimated from the MERIS and MODIS spectrometers, a low and high spatial-resolution weather model (ERA-I and WRF), and both the conventional linear and new power-law empirical methods. Our test-regions include Southern Mexico, Italy, and El Hierro. We find spectrometers give the largest reduction in tropospheric signal, but are limited to cloud-free and daylight acquisitions. We find a ~10–20% RMSE increase with increasing cloud cover consistent across methods. None of the other tropospheric correction methods consistently reduced tropospheric signals over different regions and times. We have released a new software package called TRAIN (Toolbox for Reducing Atmospheric InSAR Noise), which includes all these state-of-the-art correction methods. We recommend future developments should aim towards combining the different correction methods in an optimal manner.

1. Introduction

Interferometric Synthetic Aperture Radar (InSAR) is a geodetic tool that is well suited to the observation of crustal deformation processes. However, the use of InSAR to measure small magnitude and long wavelength deformation signals, such as interseismic slip (e.g. Fournier, Pritchard, & Finnegan, 2011; Hooper et al., 2013; Béjar-Pizarro et al., 2013; Walters, Elliott, Li, & Parsons, 2013), subduction zone slow slip events (e.g. Cavalié et al., 2013; Bekaert, Hooper, & Wright, 2015a), and creep (e.g. Jolivet et al., 2012) is severely limited by atmospheric contamination of the InSAR data. Separating deformation from atmospheric signals, introduced by the variation of atmospheric properties in space and time, remains one of the major challenges for InSAR (Hooper et al., 2013).

Atmospheric delays are typically split into ionospheric and tropospheric terms. Ionospheric effects are caused by variations in free electrons along the travel path, resulting in a phase advance of the radar signal that becomes more significant for larger wavelengths, such as for P and L-band SAR (e.g. Gray, Mattar, & Sofko, 2000). Tropospheric effects are caused by variations in pressure, temperature, and relative humidity in the lower part of the troposphere (<5 km), which

cause signals in interferograms of up to 15–20 cm in magnitude, and can often be much larger than the tectonic signals of interest (e.g. Hooper et al., 2013; Bekaert et al., 2015a). In this study, we focus on the testing and comparison of correction methods for tropospheric noise. Contamination from ionospheric noise in our test-data is minimized as we use C and X-band SAR data only.

The 2-way tropospheric phase delay, ϕ_{tropo}, at a specific height $h = h_1$, corresponds to the integration of the hydrostatic and wet component of the refractivity, N, between h_1 and the top of the troposphere, h_{top}, along the radar line-of-sight as:

$$N = \left(k_1 \frac{P}{T}\right)_{hydr} + \left(k_2' \frac{e}{T} + k_3 \frac{e}{T^2}\right)_{wet} = N_{hydr} + N_{wet}$$
$$\phi_{tropo} = \frac{-4\pi}{\lambda} \frac{10^{-6}}{\cos\theta} \int_{h_1}^{h_{top}} (N_{hydr} + N_{wet}) dh \qquad (1)$$

where P indicates total atmospheric pressure, T the temperature, e the partial pressure of water vapor, θ the incidence angle, λ the radar wavelength, and $-4\pi/\lambda$ a conversion factor to convert from pseudo-range increase to phase delay (Hanssen, 2001). The coefficients k_1, k_2' and k_3 are empirical constants which we take as $k_1 = 77.6$ K hPa^{-1}, $k_2' = 23.3$ K hPa^{-1} and $k_3 = 3.75 \cdot 10^5$ K^2 hPa^{-1} (Smith & Weintraub, 1953). For InSAR, the interferometric tropospheric phase delay $\Delta\phi_{tropo}$

* Corresponding author at: COMET, School of Earth and Environment, University of Leeds, United Kingdom.

(from now on referred to as tropospheric phase delay) is the difference between tropospheric delay at the master and slave acquisition times $\Delta\phi_{\text{tropo}} = \phi_{\text{tropo}}^{\text{slv}} - \phi_{\text{tropo}}^{\text{mst}}$, and thus depends on the change in refractivity, rather than the total refractivity.

Tropospheric corrections can be calculated using auxiliary information from weather models (e.g. Wadge et al., 2002; Liu, Hanssen, & Mika, 2009; Doin, Lasserre, Peltzer, Cavalié, & Doubre, 2009; Jolivet, Grandin, Lasserre, Doin, & Peltzer, 2011; Walters, Parsons, & Wright, 2014; Jolivet et al., 2014), GPS measurements (e.g. Williams, Bock, & Fang, 1998; Onn & Zebker, 2006; Li, Fielding, Cross, & Muller, 2006a; Löfgren et al., 2010), multi-spectral observations (e.g. from the Medium Resolution Imaging Spectrometer (MERIS) onboard the Envisat satellite; or the Moderate Resolution Imaging Spectroradiometer (MODIS) onboard the Terra and Aqua satellites) (Li et al., 2006b; Li, Fielding, Cross, & Preusker, 2009; Li, Fielding, & Cross, 2009), or GPS in combinations with spectrometer data (e.g. Li, Muller, Cross, & Fielding, 2005; Puysségur, Michel, & Avouac, 2007). The estimated corrections are often limited by the spatial and temporal resolution, and the precision of the auxiliary data. GPS stations are often absent or sparsely distributed in many areas around the world. Spectrometers can only provide useful corrections under cloud-free and daylight conditions. Weather models and spectrometer observations that are not acquired simultaneously with SAR data need to be interpolated in time, which can also introduce uncertainties. This is not required for MERIS in combination with Envisat ASAR sensor, as both were operated simultaneously onboard Envisat.

Tropospheric corrections can also be calculated empirically directly from the interferogram. Tropospheric delays $\Delta\phi_{\text{tropo}}$ for an individual interferogram can be estimated by assuming a linear relation, $\Delta\phi_{\text{tropo}} = K_{\Delta\phi}h + \Delta\phi_0$, between topography h and the interferometric phase $\Delta\phi$ in a non-deforming region (Wicks et al., 2002) or in a spatial band insensitive to deformation (Lin, Simons, Hetland, Muse, & DiCaprio, 2010), where $K_{\Delta\phi}$ is the gradient to be estimated, and $\Delta\phi_0$ is a constant that can be neglected as it merely represents a constant shift applied to the whole interferogram. Elliott, Biggs, Parsons, & Wright (2008) used a modification of this method and removed a preliminary estimate of the deformation displacements prior to estimating $K_{\Delta\phi}$. Such phase-based methods have been effective in the reduction of tropospheric signals, but are limited as they assume no spatial variability of the tropospheric properties is present. Some authors have attempted to overcome this limitation by applying a piece-wise slope correction over multiple windows (e.g. Béjar-Pizarro et al., 2013). However, this method is technically flawed, as a laterally-varying tropospheric signal requires a common reference between windows, and estimation of the constant $\Delta\phi_0$ within windows is not possible as other phase contributions bias the estimate. Alternatively, Bekaert, Hooper, & Wright (2015b) developed a power-law model, which unlike the linear approach can account for a spatially-varying tropospheric signal in the presence of deformation.

In this study, we perform a statistical analysis of several different tropospheric correction methods that can be used to correct an individual interferogram. This includes corrections estimated from (i) MERIS at ~1.2 km spatial-resolution, (ii) MODIS at 1 km resolution, (iii) the archived European Center for Medium-Range Weather Forecasts (ECMWF) ERA-I weather model at 80 km resolution (Dee et al., 2011), (iv) a locally run Weather Research and Forecasting Model (WRF) (Michalakes et al., 2004) nested to a 7 km resolution, and the phase-based empirical (v) linear and (vi) power-law corrections. All these methods are included in TRAIN, our open-source Toolbox for Reducing Atmospheric InSAR Noise.

2. Tropospheric correction methods for InSAR

Tropospheric signals consist of a short-scale (few km) component, introduced by turbulent as well as coherent dynamics in the troposphere, a longer-scale (10 s of km) component, introduced by lateral

variation of pressure, temperature and humidity, and a topography-correlated component due to changes of pressure, temperature, and relative humidity with height (e.g. Hanssen, 2001). Different correction techniques have different sensitivities for these three components of the tropospheric delay. For example, weather models often have timing issues, which render them unable to correctly resolve the turbulent variation of water vapor (e.g. Liu et al., 2009). While the statistical properties of the turbulent component can be representative for the region, the location can be wrong, leading to an adverse effect when removing the estimated tropospheric signal. Unlike water vapor, temperature and pressure are smooth in space, leading to a better-resolved longer wavelength hydrostatic component. Spectrometer measurements only produce an estimate for the wet component of the delay. While a direct comparison is possible between the spectrometer correction and the wet delay as estimated from weather models, the phase-based methods cannot produce separate wet and hydrostatic components of the delay. As the linear and the power-law methods only estimate a topography-correlated component of the delay, they explicitly cannot account for the turbulent and coherent short-scale component.

In the following section we provide more information on the estimation procedure of the different correction methods.

2.1. Tropospheric delays from weather models

The output (pressure, temperature, and relative humidity) from local or global weather models can be used with Eq. (1) to compute both hydrostatic and wet tropospheric delay (Doin et al., 2009; Jolivet et al., 2011). In this study we used the freely available archived ERA-I global model, and also run our own local high spatial-resolution model using the Weather Research and Forecasting (WRF) model (Michalakes et al., 2004).

ERA-I outputs data at a spatial resolution of ~80 km, at a 6 h interval, and on 37 pressure levels (Dee et al., 2011). We performed a lateral and vertical spline interpolation of pressure, temperature, and relative humidity, after which we computed the refractivity and the integration from the surface upwards. To match the SAR acquisition time, we performed a linear interpolation in time.

We modified the WRF set-up to produce outputs at the same 37 pressure levels as ERA-I. We set the boundary of the parent WRF domain using the National Center for Environmental Prediction (NCEP) Climate Forecast System Reanalysis (CFSR) data (Saha et al., 2010) and NCEP's Global Forecast System analysis (GFS) (Unidata et al., 2003). As GFS did not exist prior to 1 November 2006, we used the CFSR data instead for those dates. The impact of changing between CFSR and GFS on the estimated delays is small. We estimate negligible differences in slant total delay between the two methods; the average RMS difference is <1 mm across 15 interferograms for which CFSR and GFS corrections were both available.

2.2. Tropospheric delays from spectrometer observations

Both MERIS and MODIS provide products of Precipitable Water Vapor (PWV), the vertically integrated water vapor content of the atmosphere. The MERIS estimate for PWV is computed by comparing the radiance ratio between two closely-spaced infrared frequency bands, of which only one is sensitive to water vapor (ESA, 2011). A similar approach is used for MODIS but with five near-infrared bands instead (Gao & Kaufman, 2003). PWV is defined as the equivalent column height of liquid water when integrating all water vapor e from the surface h to the top of the atmosphere (Bevis et al., 1992):

$$\text{PWV} = \frac{1}{\rho_w R_v} \int_h^\infty \frac{e}{T} \text{d}h, \qquad (2)$$

where ρ_w is the density of water, R_v the specific gas constant of water vapor, and T temperature. The MERIS PWV accuracy has been estimated

from continuous GNSS to be ~1.1 mm, equivalent to ~6.2 mm of zenith wet delay for each epoch (Li et al., 2006b). For a difference between two epochs this increases by a factor of $\sqrt{2}$ to 8.8 mm. This is equivalent to ~1 cm in radar line-of-sight for Envisat with an incidence angle of 23°, obtained by substituting PWV = 8.8 mm in the computation of the spectrometer delay, Eq. (5), provided below. We found that MODIS gives at best an accuracy equal to that of MERIS, and at worst twice that of MERIS, further detailed in the results section. MERIS has no bias in PWV retrieval, but MODIS tends to over-estimate PWV on average by 5% (Li, Muller, & Cross, 2003). For those SAR dates where PWV from MERIS and MODIS have ≥50% mutual pixels after applying a cloud cover mask, we estimated a MODIS recalibration factor α_{MODIS} from a linear relation between both the cloud-free MERIS and MODIS PWV. For the other SAR acquisitions we assumed the calibration factor to be the weighted average of the estimated calibration factors, where weights were estimated from bootstrapping.

The tropospheric delay of Eq. (1) can be rewritten as:

$$\phi_{tropo}^{wet} = \frac{-4\pi}{\lambda} \frac{10^{-6}}{\cos\theta} \left(k_2' \int_{h_1}^{h_{top}} \frac{e}{T} dh + \frac{k_3}{T_m} \int_{h_1}^{h_{top}} \frac{e}{T} dh \right) \quad (3)$$

where T_m is (Davis, Herring, Shapiro, Rogers, & Elgered, 1985):

$$T_m = \frac{\int_h^\infty e/T \, dh}{\int_h^\infty e/T^2 \, dh}. \quad (4)$$

This can now be further rewritten in terms of the spectrometer delay as:

$$\phi_{tropo}^{wet} = \frac{-4\pi}{\lambda} \frac{\Pi}{\cos\theta} * PWV, \quad (5)$$

where Π is a conversion factor (Bevis et al., 1992; Niell et al., 2001; Li et al., 2003; Li et al., 2006b), typically around 6.2, that varies with the temperature of the troposphere, as:

$$\Pi = R_v \rho_w 10^{-6} \left(k_2' + \frac{k_3}{T_m} \right). \quad (6)$$

We estimate Π for individual SAR acquisitions using balloon sounding data, provided by the Department of Atmospheric Science of the University of Wyoming.

2.3. Phase-Based tropospheric delays

The interferometric tropospheric phase $\Delta\phi_{tropo}$ can be estimated from the relationship between the interferometric phase and the topography as:

$$\Delta\phi_{tropo} = K_{\Delta\phi} h + \Delta\phi_0, \quad (7)$$

for the linear method, and

$$\Delta\phi_{tropo} = K_{\Delta\phi}' (h_0 - h)^\alpha, \quad \text{with} \quad h < h_0 \quad (8)$$

for the power-law method, where $K_{\Delta\phi}$ and $K_{\Delta\phi}'$ are coefficients relating phase to topography. The power-law reference height, h_0, and the power-law coefficient, α, are constants estimated from balloon sounding data, or weather model data (Bekaert et al., 2015b). Unlike the linear method, the power-law method can account for spatial variation of tropospheric properties by estimating $K_{\Delta\phi}'$ over local windows.

Lateral variation for the lower part of the troposphere is critically controlled by the interaction of air parcels with topographic barriers (Markowski & Richardson, 2010). Whether or not an air parcel will

flow around or over a mountain is related to the relative height, the slope of the mountain, the mountain aspect ratio, the horizontal wind speed towards the mountain, and the static stability of the troposphere. The stagnation height, h_{stag}, or the mountain height for which blockage occurs, can be simplified as:

$$h_{stag} = \frac{v_m}{f_{bv}} \quad (9)$$

with v_m horizontal wind speed towards the mountain, and f_{bv} the Brunt–Väisälä frequency (Markowski & Richardson, 2010), which we fixed to be 0.01 Hz.

The original power-law method (Bekaert et al., 2015b) splits the study region into multiple rectangular windows, over which the local phase-topography relation is estimated. This is then interpolated to all data points, by weighting the windows with the distance to the data points, and with the window uncertainty of the estimate. We modified the method to account for disconnected tropospheric regions by specifying a physical boundary, identified from stagnation or mountain blockage, which is used to limit the interpolation to the windows of the same tropospheric region only.

First, we computed the stagnation height for each SAR date using WRF, and compared stagnation height with local topography to identify disconnected regions. Figs. S1–S3 give a binary representation for all SAR dates whether or not stagnation occurs. Second, we combined the binary information of all SAR dates to compute the fraction of consistent stagnation over time (Fig. 1), which allows us to identify the physical boundaries that act as barriers persistently through time.

3. InSAR processing

We processed InSAR data using ROI_PAC to focus the raw data (Rosen, Henley, Peltzer, & Simons, 2004), DORIS to form interferograms (Kampes, Hanssen, & Perski, 2003), and StaMPS to select stable scatterer pixels (Hooper, Segall, & Zebker, 2007). While a time-series InSAR approach is not required to estimate the tropospheric delay map for each individual interferogram, it allowed us to increase the signal-to-noise ratio, helping the unwrapping process. Moreover, when processed though a small baseline network, it allowed us to validate the unwrapping process. Known phase contributions due to Envisat's oscillator drift are also removed according to Marinkovic & Larsen (2015).
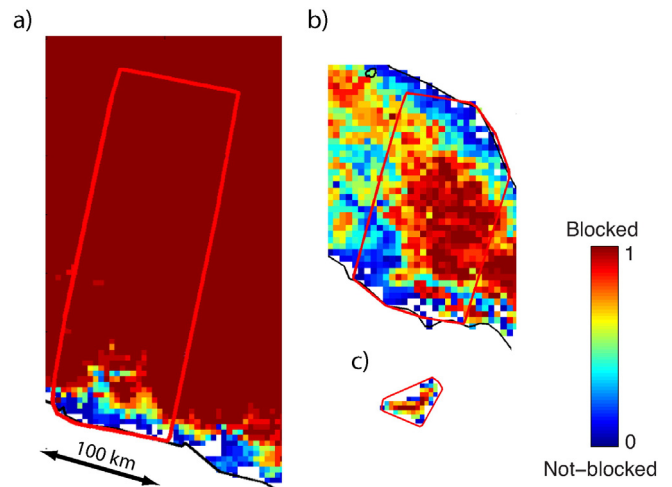

Fig. 1. Fraction of consistent mountain blockage over time for (a) Mexico, (b) Italy, and (c) El Hierro, using WRF wind velocities at the time and date of the SAR acquisitions. Mountain blockage for individual SAR acquisitions is contained in Figures S1–S3 for the different regions. (See the online manuscript for a full color version of this figure)

4. Background of the test sites

We investigated the correction capability of the different tropospheric InSAR correction methods over three test sites: Mexico, Italy, and El Hierro in the Canary Islands (Fig. 2).

Over Mexico we generated a single master network of 19 descending Envisat interferograms (track 255, Table S1), spanning the period from November 2004 until December 2009, and covering an area of ~100 km by 340 km. While no significant earthquakes occurred during our study, interferograms are subjected to long-wavelength (few 100 s km) tectonic displacements introduced by the 2006 Guerrero slow slip event, equivalent to M_w ~ 7.3 (Bekaert et al., 2015a), as well as interseismic deformation due to locking on the subduction interface.

The topography ranges from sea-level up to 4.8 km elevation, and includes The Valley of Mexico City, and the surrounding Popocatépetl and Iztaccihuatl volcanoes. A mountain range of ~2 km elevation, just 100 km inland from the coast, acts as an obstacle for air flow and thus can introduce different atmospheric conditions on either side of the mountain. Large tropospheric phase delays (>5 cm) have been observed in previous InSAR studies of this region (e.g. Hooper, Bekaert, Spaans, & Arikan, 2012; Cavalié et al., 2013; Bekaert et al., 2015b).

Over Italy we generated a small baseline network of 49 descending Envisat interferograms (track 79, Table S2), spanning December 2002 until February 2009. Our study area extends from the western to eastern coastline of peninsular Italy (~100 km by 260 km), crossing the Apennines, with a maximum topographic height of ~2 km and ridges oriented parallel with the coastline. Within this region six earthquakes of $M_w \geq 5$ occurred, clustered around April 2009, of which the L'Aquila earthquake of 6 April was the largest with M_w 6.3 (e.g. Walters et al., 2009; Cheloni et al., 2014). Tectonic contamination from long-wavelength (few 100 s km) interseismic deformation (extension rate of 6 ± 2 mm/yr. D'Agostino, Giuliani, Mattone, & Bonci, 2001) is expected to be small, as horizontal deformation is predominately perpendicular to the radar line-of-sight, in which direction InSAR is insensitive.

Over El Hierro we generated a small baseline network of 78 descending TerraSAR-X interferograms (track 79, Table S3). El Hierro is much smaller (~30 km by 25 km) than our Mexico and Italy datasets, and as an island is completely surrounded by water. The local topography is related to the volcanic nature of the island. A sharp cliff ~1.5 km high, in combination with the surrounding ocean, allows for complex and highly turbulent tropospheric delays. Our InSAR data covers the period from September 2011 until February 2012, and includes the 13 October 2011 submarine eruption (e.g. González et al., 2013).

5. Results and discussion

Prior to the computation of the MODIS tropospheric delays, we performed a recalibration of MODIS PWV using MERIS as a reference. The left panel of Fig. S4 shows the estimated calibration factors α_{MODIS} for individual SAR acquisitions, with the uncertainty estimated from 1200 bootstrap runs. The average uncertainty for α_{MODIS} is 0.001. The average weighted calibration factor amounts to ~0.98 over Italy, based on 13 samples, and ~0.95 over Mexico, using only 14 samples, or when combining all samples (Fig. S4 right panel). This value is in agreement with Li et al. (2003) and Li et al. (2005), who found an average recalibration factor of 0.95 when comparing MODIS PWV with GPS observations over Germany and Southern California. On average we found negligible differences between estimated tropospheric delays when applying an individual estimated calibration factor or when assuming a fixed value of 0.95. Therefore we believe it will be sufficient for future studies to estimate a single calibration factor for each region.

The power-law method can be applied in deforming regions by applying the estimation in a spatial band insensitive to the deformation. However, other strong signal contamination from the turbulent troposphere and orbit errors should also be avoided. While turbulent signals manifest at short spatial scales, and orbit errors are of long wavelength, the selection of the non-deforming band is not always trivial, as it requires a priori information about the spatial extent of deformation throughout time.

We selected the spatial band whose correction had the smallest RMSE when compared to the unwrapped interferograms (Fig. S5). To avoid contamination of deformation, we corrected the interferograms (left panel) for a time-series estimate of tectonic deformation and DEM errors.

We found the mean RMSE to vary more strongly between spatial bands over Mexico (σ_{RMSE} of 0.2 cm) and Italy (σ_{RMSE} of 0.3 cm), than over El Hierro ($\sigma_{RMSE} < 1$ mm). The 8–16 km spatial band corresponded to the smallest RMSE over Mexico, 16–32 km over Italy, and 4–16 km over El Hierro.

We modified the power-law method from Bekaert et al. (2015a) to allow for disconnected tropospheric regions separated by blue solid lines in Fig. 2, which likely have different tropospheric conditions. To
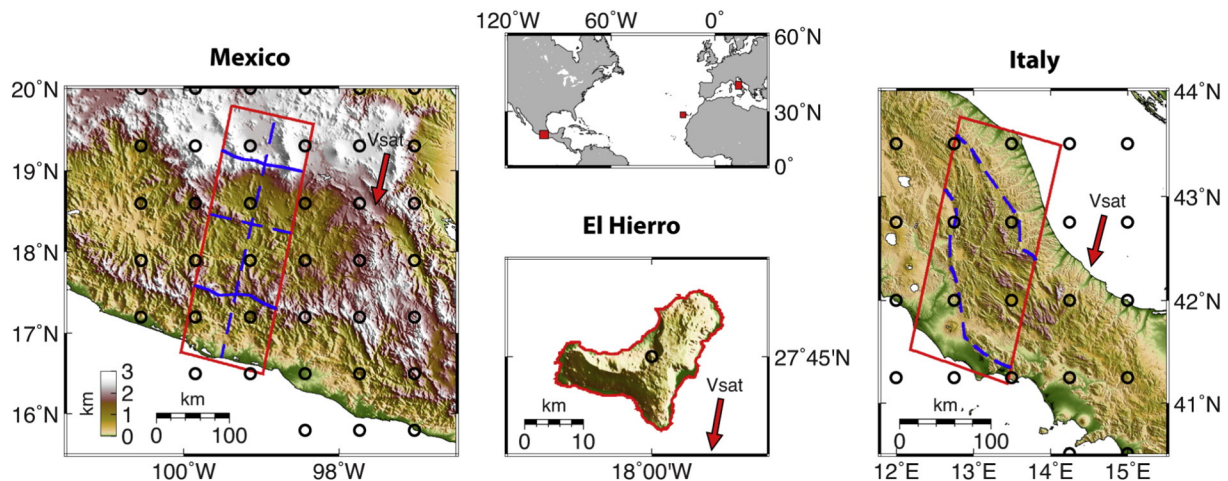

Fig. 2. Overview map (center) with inserts of our study regions: Mexico, Italy, and El Hierro. Map colors show the local topography from the Shuttle Radar Topography Mission, saturated at 3 km elevation. Red polygons indicate the illuminated ground area of the descending InSAR data. Solid blue lines define a border between different tropospheric regions, as found from consistent wind stagnation over time due to local topography (Fig. 1). Together, blue solid and blue dashed lines define the local windows as used for the power-law correction method, where windows within a tropospheric region constrain the delay estimation. Black circular markers indicate the location of the ERA-I weather model data points, at ~75 km spatial resolution. To avoid clutter, the high resolution WRF model points are not shown; we used a spatial resolution of 7 km over Mexico and Italy, and 2 km over El Hierro. (See the online manuscript for a full color version of this figure)

identify these regions we used Eq. (9) to compute the consistency of wind stagnation over time due to topography (Fig. 1).

Mountain blockage occurs for more than 95% of the time over our Mexican study area, except for the region within ~10 km of the Mexican coast, dividing our study area into multiple disconnected tropospheric regions. We did not enforce different disconnected regions over Italy, as the western extent of our study region is only blocked 50–65% of the time. Over El Hierro this analysis is not applicable due to its smaller extent. The identification of different disconnected tropospheric regions (Fig. 2, blue solid lines), in combination with local subdivision to allow for spatial variation of tropospheric properties (blue dashed lines), leads to a total of eight power-law windows over Mexico, three over Italy, and one over El Hierro.

Fig. 3(a)–(c) shows two examples of the estimated tropospheric delays for the different correction methods for each test-region. For each of these three regions, the first example (Case 1) shows a scenario where the tropospheric delays are mainly topography-correlated. We find

that all methods show both a similar magnitude of the estimated delay and a similar spatial pattern of the delay.

The second example (Case 2) demonstrates a more complex tropospheric delay, with spatial variation of tropospheric properties and with a significant turbulent behavior of the troposphere. Variation can be observed between the different estimated delays, especially over Mexico and Italy. Both MERIS and MODIS estimated delays show a strong resemblance to the original interferograms, whereas the weather model correction shows delays of similar order of magnitude, but not always correctly located (e.g. over Mexico). As the phase-based (linear and power-law) methods are estimated over a region, they are incapable of matching the turbulent signals. Over El Hierro the effect of long wavelength spatial variation is limited due to the small extent of the island, hence the main variation in the tropospheric signal results from the topography-correlated signal and turbulence. While the high-resolution weather model (WRF) is capable of capturing the correct spatial trend over
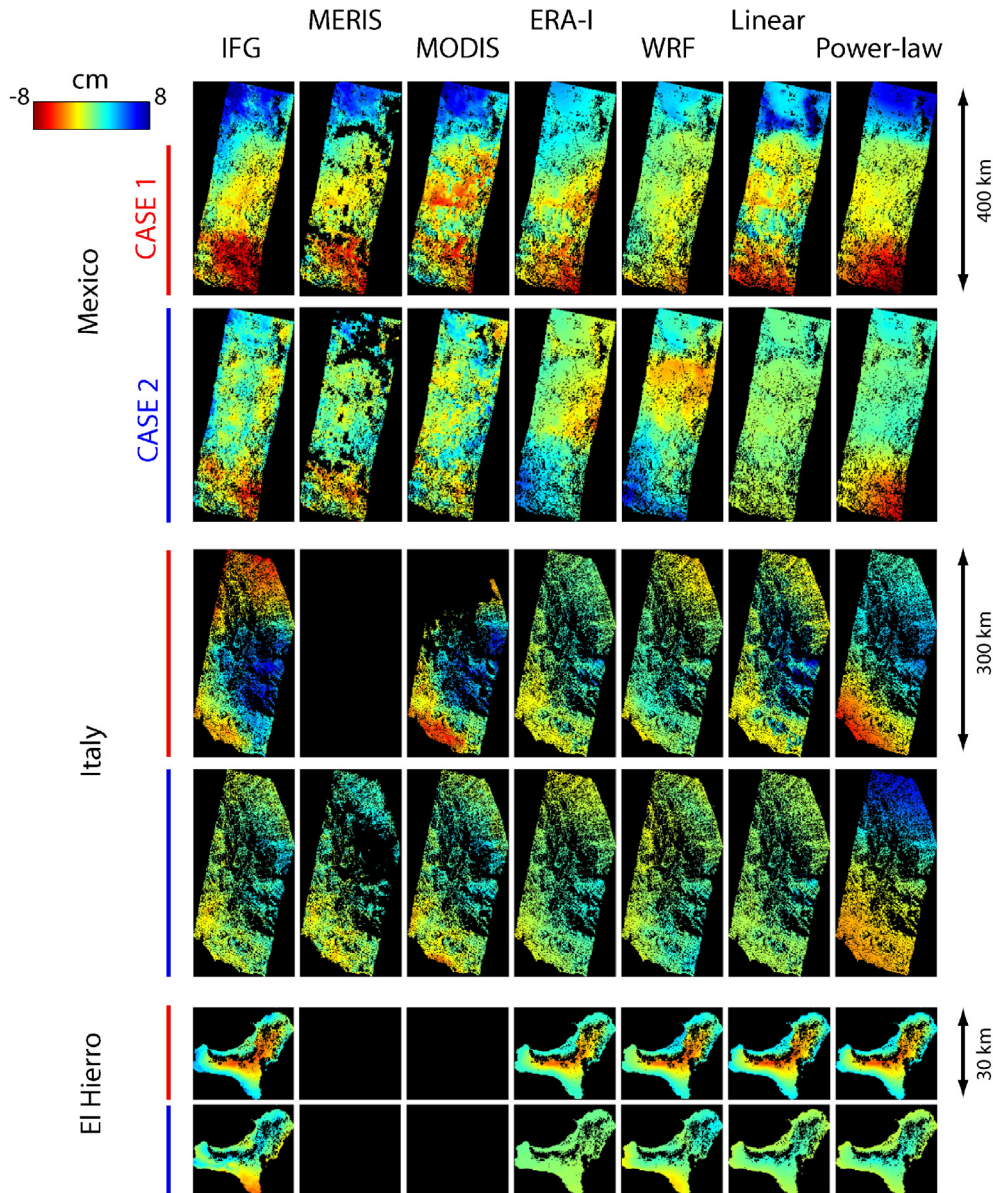

Fig. 3. Example of tropospheric delay estimates for different correction methods over Mexico, Italy, and El Hierro. Two examples are shown for each region. Case 1 (red) corresponds to an example where the tropospheric delay is mainly correlated with the topography. Case 2 (blue) represents an example with a more complex, turbulent and or spatially-varying tropospheric signal. Columns give from left to right, the unwrapped interferogram, and the estimated tropospheric corrections using MERIS, MODIS, ERA-I, WRF, the linear method, and when using the power-law method. Both MERIS and MODIS spectrometers also have a hydrostatic component of ERA-I included to allow one for comparison with the phase-based correction methods. All observations are converted to displacements in the radar line-of-sight. (See the online manuscript for a full color version of this figure)

the region, it cannot capture the high gradients in the delay from tur-bulence (few km). Spectrometer estimates of MERIS and MODIS were not included over El Hierro due to limited amount of data, but when they were available their estimated delays were limited by their lower, ~1 km, spatial resolution.

For each region we performed a statistical analysis where we com-pared all the tropospheric techniques with respect to the unwrapped in-terferograms (Fig. 4), similar to the analysis used for the power-law spatial band selection. As before, the left panel gives the RMS of the unwrapped interferograms, while the right panel gives the RMSE of the different tropospheric correction methods after subtracting the cor-rections from the unwrapped interferograms.

Assuming the unwrapped interferograms are correctly compensated for signals other than the troposphere, the maximum reduction in RMSE will be limited by the accuracy of the tropospheric correction method under consideration. For MERIS this corresponds to a RMSE level of ~1 cm (black line), computed using the measured ~1.1 mm PWV accu-racy (Li et al., 2006b).

In order not to limit ourselves to cloud free interferograms only, we split our dataset into three classes: interferograms in which both SAR dates are cloud-free (triangular markers), those in which one of the SAR dates fails our 80% cloud-free threshold (circular markers), and those where both SAR dates fails our cloud-free threshold (diamond markers). By comparing the different classes, we observe all correction methods perform worse as cloud cover increases. On average we find a 10–20% RMSE increase for each additional cloudy SAR date, for all the methods.

Over the different regions, we find MERIS consistently gives the larg-est RMSE reduction, resulting in RMSE approximately equal to the MERIS ~1 cm accuracy level (black line). No uncertainty is introduced through temporal interpolation for MERIS, unlike for MODIS. Over Italy and Mexico, we find MODIS acquisitions are on average within ~25 min ($\sigma = 18$ min) of our SAR acquisition times, with a maximum time difference of around an hour. While both MERIS and MODIS have similar sensitivities, MODIS does not perform as well over Mexico,

reducing the RMSE to only ~2 cm (twice as bad than the MERIS accura-cy), while over Italy MODIS performs similarly to MERIS. While spec-trometers are the preferred method in terms of RMSE reduction, the success-rate is limited to cloud-free and daylight acquisitions only. This excludes the use of spectrometer data for the correction of ascend-ing SAR data for satellite systems in a sun-synchronous orbit with night-time ascending acquisitions, such as Envisat (ascending node at 22:00 local time at the equator), ERS 1/2 (22:28 at equator), ALOS (22.00 at equator), and ALOS2 (00:00 at equator). However, for SAR systems which operate in a sun-synchronous dawn-dusk orbit, such as Sentinel 1, Radarsat, Radarsat 2, the future NISAR mission (ascending node at 18:00 for all), and COSMO-SkyMed (ascending node at 06:00), spectrometer-derived corrections can potentially be used for both as-cending and descending acquisitions. The application to ascending and descending tracks for these satellites is limited by variation in the length of day over winter and summer seasons, and as such will also be strong-ly influenced by the latitude of the target.

For Mexico and El Hierro, phase-based methods give a better RMSE reduction than weather models, and in the case of Mexico are also bet-ter than the MODIS spectrometer. Over Italy we find that none of the dif-ferent methods, except for the spectrometers, reduces the RMSE on average.

With large topographic variations over Mexico, the main tropo-spheric signal contribution results from the topography-correlated component. The phase-based methods, especially designed to resolve the topography-correlated component, therefore are capable of retriev-ing the tropospheric delay, reducing the RMSE by 0.5 cm to an average RMSE level of 1.9 cm. Over Italy, tropospheric delays are more subject to signals introduced from local weather and turbulent variations, which results in a strongly under estimated tropospheric signal from the linear method with a maximum RMSE reduction of only ~0.05 cm on cloud-free interferograms, and 0.3 cm for the complete dataset to an average RMSE level of 1.2 cm. As the power-law is applied locally, it is more strongly contaminated by the different tropospheric delay components, which are present at different spatial scales, leading to a
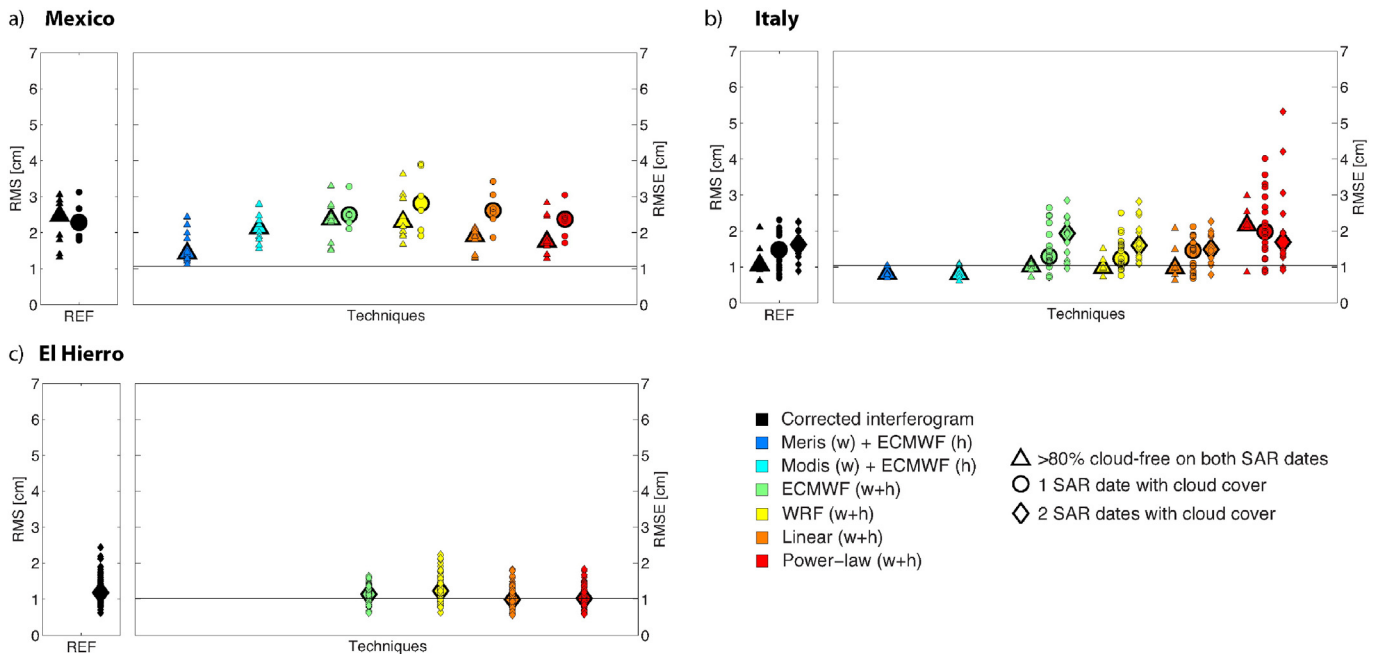

Fig. 4. Statistical analysis between different tropospheric correction methods over (a) Mexico, (b) Italy, and (c) El Hierro. Left panel, Root Mean Squared (RMS) of the tropospheric signal of the reference technique, corresponding to the unwrapped interferograms corrected for DEM errors and tectonic signals. Right panel, RMS Errors after correction of the reference signal using tropospheric estimates of the power-law for different spatial bands (colored markers). Triangular markers corresponds to interferograms that are more than 80% cloud free, circular markers to interferograms for which one of the SAR dates had more than 20% clouds, and diamond markers where both SAR dates failed the cloud-free threshold. Small colored markers represent individual interferograms, while the thicker marker represents the average of all interferograms. The solid line gives the expected MERIS accuracy level. Wet delay components are indicated by (w), and hydrostatic components by (h). (See the online manuscript for a full color version of this figure)

biased estimation of $K_{\Delta\phi}'$, and an average RMSE increase of ~0.2 cm. This is also expressed by the large RMSE across the different power-law spatial bands (Fig. S5). Considering both phase-based methods have the potential to introduce incorrect signals in the presence of turbulence and coherent short-scale tropospheric signals, neither should be applied in those instances. However, for the linear correction method the impact of turbulence appears less severe than for the power-law method.

We do not observe an improvement by running a local high-resolution weather model. This can be observed at El Hierro, where the high-resolution model tries to estimate turbulence, but due to its incorrectly estimated location, is penalized with a larger RMSE. With high-resolution models offering only a minimal improvement and requiring additional computation, online available weather models are more suitable for near real-time InSAR processing.

Preferred correction methods depend on the region of application and the SAR satellite under consideration. However, from our analysis we find that each method has its limitations, which vary with region of application and with time. For future development we suggest that it would be optimal to combine the different correction methods in such a way that they can constrain each other. Further work is needed in order to identify suitable metrics that can be used to weight the different observations.

6. Conclusions

We performed a statistical comparison of different tropospheric correction methods with respect to unwrapped interferograms over Mexico, Italy, and El Hierro. Our analysis included methods based on spectrometer measurements, output of weather models, and empirical interferometric phase-based methods. When available and limited to cloud-free and daylight acquisitions only, we found the spectrometers to provide the largest RMSE reduction. We found that the estimated tropospheric delays using MODIS have at best an accuracy equal to that of MERIS, and at worst twice that of MERIS. We found the phase-based methods (linear and power-law) to outperform the weather model methods in regions where tropospheric delays are mainly correlated with topography. For regions over which this is less apparent, due to turbulence in the troposphere and dynamic local weather, weather models can potentially offer better performance. In those instances where weather models mis-estimate the location of turbulent features, they will have a correspondingly higher RMSE. We did not find a significant improvement when using a local high-resolution weather model (7 km and 2 km) instead of the global reanalysis products. With a longer required runtime, local weather model are less suitable for near real-time InSAR application. From a cloud cover analysis, we found the performance of the different correction methods to worsen with increasing cloud cover, with a ~10–20% increase in RMSE for each cloudy SAR date.

We confirmed that the different tropospheric correction techniques all have their own limitations, and are not always sensitive to the same component of the tropospheric delay. We did not find any of the tropospheric correction methods to be best in reducing the tropospheric delays consistently over different regions and times. Therefore, we recommend future developments should aim towards combining the different correction methods in an optimal manner.

Together with this paper we release the Toolbox for Reducing Atmospheric InSAR Noise - TRAIN, which contains all the applied correction methods within this study. In future we will further expand this toolbox to include other corrections, such as those from GPS.

Appendix A. Supplementary data

Supplementary data to this article can be found online at http://dx.doi.org/10.1016/j.rse.2015.08.035.

References

Béjar-Pizarro, M., Socquet, A., Armijo, R., Carrizo, D., Genrich, J., & Simons, M. (2013). Andean structural control on interseismic coupling in the North Chile subduction zone. *Nature Geoscience*, 6, 462–467. http://dx.doi.org/10.1038/NGEO1802.

Bekaert, D., Hooper, A., & Wright, T. (2015a). Reassessing the 2006 Guerrero slow slip event, Mexico: implications for large earthquakes in the Guerrero Gap. *Journal of Geophysical Research*, 120. http://dx.doi.org/10.1002/2014JB011557.

Bekaert, D., Hooper, A., & Wright, T. (2015b). A spatially variable power law tropospheric correction technique for InSAR data. *Journal of Geophysical Research*, 120http://dx.doi.org/10.1002/2014JB011558.

Bevis, M., Businger, S., Herring, T., Rocken, C., Anthes, R., & Ware, R. (1992). GPS meteorology: Remote sensing of atmospheric water vapor using the global positioning system. *Journal of Geophysical Research*, 97, 15,787–15,801. http://dx.doi.org/10.1029/92JD01517.

Cavalié, O., Pathier, E., Radiguet, M., Vergnolle, M., Cotte, N., Walpersdorf, A. Cotton, F. (2013). Slow slip event in the Mexican subduction zone: evidence of shallower slip in the Guerrero seismic gap for the 2006 event revealed by the joint inversion of InSAR and GPS data. *Earth and Planetary Science Letters*, 367. http://dx.doi.org/10.1016/j.epsl.2013.02.020.

Cheloni, D., Giuliani, R., D'Anastasio, E., Atzori, S., Walters, R., Bonci, L. Stefanelli, G. (2014). Coseismic and post-seismic slip of the 2009 L'Aquila (central Italy) Mw 6.3 earthquake and implications for seismic potential along the Campotosto fault from joint inversion of high-precision levelling, InSAR and GPS data. *Tectonophysics*, 622, 168–185. http://dx.doi.org/10.1016/j.tecto.2014.03.009.

D'Agostino, N., Giuliani, R., Mattone, M., & Bonci, L. (2001). Active crustal extension in the Central Apennines (Italy) inferred from GPS measurements in the interval 1994–1999. *Geophysical Research Letters*, 28, 2121–2124. http://dx.doi.org/10.1029/2000GL012462.

Davis, J., Herring, T., Shapiro, I., Rogers, A., & Elgered, G. (1985). Geodesy by radio interferometry: effects of atmospheric modeling errors on estimates of baseline length. *Radio Science*, 20, 1593–1607. http://dx.doi.org/10.1029/RS020i006p01593.

Dee, D.P., Uppala, S.M., Simmons, A.J., Berrisford, P., Poli, P., Kobayashi, S.Vitart, F. (2011). The ERA-interim reanalysis: configuration and performance of the data assimilation system. *Quarterly Journal of the Royal Meteorological Society*, 137, 553–597. http://dx.doi.org/10.1002/qj.828.

Doin, M., Lasserre, C., Peltzer, G., Cavalié, O., & Doubre, C. (2009). Corrections of stratified tropospheric delays in SAR interferometry: validation with global atmospheric models. *Journal of Applied Geophysics*, 69, 35–50. http://dx.doi.org/10.1016/j.jappgeo.2009.03.010.

Elliott, J., Biggs, J., Parsons, B., & Wright, T. (2008). InSAR slip rate determination on the Altyn Tagh Fault, northen Tibet, in the presence of topographically correlated atmospheric delays. *Geophysical Research Letters*, 35. http://dx.doi.org/10.1029/2008GL033659.

ESA (2011). MERIS Level 2 Detailed Processing Model. *Technical Report PO-TN-MEL-GS-0006. European Space Agency. Issue 8, Rev 0B.*

Farr, T., Rosen, P., Caro, E., Crippen, R., Duren, R., Hensley, S. Alsdorf, D. (2007). The Shuttle Radar Topography Mission. *Reviews of Geophysics*, 45. http://dx.doi.org/10.1029/2005RG000183.

Fournier, T., Pritchard, M., & Finnegan, N. (2011). Accounting for atmospheric delays in InSAR data in a search for long-wavelength deformation in South America. *IEEE Transactions on Geoscience and Remote Sensing*, 49, 3856–3867. http://dx.doi.org/10.1109/TGRS.2011.2139217.

Gao, B., & Kaufman, Y.J. (2003). Water vapor retrievals using Moderate Resolution Imaging Spectroradiometer (MODIS) near-infrared channels. *Journal of Geophysical Research*, 108. http://dx.doi.org/10.1029/2002JD003023.

González, P.J., Samsonov, S.V., Pepe, S., Tiampo, K.F., Tizzani, P., Casu, F. Sansosti, E. (2013). Magma storage and migration associated with the 2011–2012 El Hierro eruption: Implications for crustal magmatic systems at oceanic island volcanoes. *Journal of Geophysical Research*, 118, 4361–4377. http://dx.doi.org/10.1002/jgrb.50289.

Gray, A.L., Mattar, K.E., & Sofko, G. (2000). Influence of ionospheric electron density fluctuations on satellite radar interferometry. *Geophysical Research Letters*, 27, 1451–1454. http://dx.doi.org/10.1029/2000GL000016.

Hanssen, R.F. (2001). Remote Sensing and Digital Image Processing. In F. van der Meer (Ed.), *Radar Interferometry: Data interpretation and error analysis. Earth and Environmental Science, vol. 2,* . Dordrecht, The Netherlands: Kluwer Academic Plublishers.

Hooper, A., Bekaert, D., Spaans, K., & Arikan, M. (2012). Recent advances in SAR interferometry time series analysis for measuring crustal deformation. *Tectonophysics*, 514-517, 1–13. http://dx.doi.org/10.1016/j.tecto.2011.10.013 (URL: http://www.sciencedirect.com/science/article/pii/S0040195111004343).

Hooper, A., Pietrzak, J., Simons, W., Cui, H., Riva, R., Naeije, M. Socquet, A. (2013). Importance of horizontal seafloor motion on tsunami height for the 2011 Mw = 9.0 Tohoku-Oki earthquake. *Earth and Planetary Science Letters*, 361, 469–479. http://dx.doi.org/10.1016/j.epsl.2012.11.013.

Hooper, A., Segall, P., & Zebker, H. (2007). Persistent scatterer interferometric synthetic aperture radar for crustal deformation analysis, with application to Volcán Alcedo, Galápagos. *Journal of Geophysical Research*, 112. http://dx.doi.org/10.1029/2006JB004763.

Jolivet, R., Agram, P.S., Lin, N., Simons, M., Doin, M., Peltzer, G., & Li, Z. (2014). Improving InSAR geodesy using Global Atmospheric Models. *Journal of Geophysical Research*, 119, 2324–2341. http://dx.doi.org/10.1002/2013JB010588.

Jolivet, R., Grandin, R., Lasserre, C., Doin, M., & Peltzer, G. (2011). Systematic InSAR tropospheric phase delay corrections from global meteorological reanalysis data. *Geophysical Research Letters*, 38. http://dx.doi.org/10.1029/2011GL048757.

Jolivet, R., Lasserre, C., Doin, M., Guillaso, S., Peltzer, G., Dailu, R. Xu, X. (2012). Shallow creep on the Haiyuan Fault (Gansu, China) revealed by SAR Interferometry. *Journal of Geophysical Research*, 117. http://dx.doi.org/10.1029/2011JB008732.

Kampes, B., Hanssen, R., & Perski, Z. (2003). Radar interferometry with public domain tools. *Proceedings Fringe 2003* (pp. 6).

Li, Z., Fielding, E., & Cross, P. (2009a). Integration of InSAR time-series analysis and water-vapor correction for mapping Postseismic motion after the 2003 Bam (Iran) earthquake. *IEEE Transactions on Geoscience and Remote Sensing*, 47, 3220–3230. http://dx.doi.org/10.1109/TGRS.2009.2019125.

Li, Z., Fielding, E., Cross, P., & Muller, J. (2006b). Interferometric synthetic aperture radar atmospheric correction: GPS topography-dependent turbulence model. *Journal of Geophysical Research*, 111. http://dx.doi.org/10.1029/2005JB003711.

Li, Z., Fielding, E., Cross, P., & Preusker, R. (2009b). Advanced InSAR atmospheric correction: MERIS/MODIS combination and stacked water vapour models. *International Journal of Remote Sensing*, 30, 3343–3363. http://dx.doi.org/10.1080/01431160802562172.

Li, Z., Muller, J., & Cross, P. (2003). Comparison of precipitable water vapor derived from radiosonde, GPS, and Moderate-Resolution Imaging Spectroradiometer measurements. *Journal of Geophysical Research*, 108. http://dx.doi.org/10.1029/2003JD003372.

Li, Z., Muller, J., Cross, P., Albert, P., Fischer, J., & Bennartz, R. (2006a). Assessment of the potential of MERIS near — infrared water vapour products to correct ASAR interferometric measurements. *International Journal of Remote Sensing*, 27, 349–365. http://dx.doi.org/10.1080/01431160500307342.

Li, Z., Muller, J., Cross, P., & Fielding, E. (2005). Interferometric synthetic aperture radar (InSAR) atmospheric correction: GPS, Moderate Resolution Imaging Spectroradiometer (MODIS), and InSAR integration. *Journal of Geophysical Research*, 110. http://dx.doi.org/10.1029/2004JB003446.

Lin, Y., Simons, M., Hetland, E., Muse, P., & DiCaprio, C. (2010). A multiscale approach to estimating topographically correlated propagation delays in radar interferograms. *Geochemistry, Geophysics, Geosystems*, 11.

Liu, S., Hanssen, R., & Mika, A. (2009). On the value of high-resolution weather models for atmospheric mitigation in SAR interferometry. *Geoscience and Remote Sensing Symposium, 2009 IEEE International, IGARSS 2009* (pp. II-749–II-752). http://dx.doi.org/10.1109/IGARSS.2009.5418199.

Löfgren, J., Björndahl, F., Moore, A., Webb, F., Fielding, E., & Fishbein, E. (2010). Tropospheric correction for InSAR using interpolated ECMWF data and GPS Zenith Total Delay from the Southern California Integrated GPS Network. *Geoscience and Remote*

Sensing Symposium (IGARSS), 2010 IEEE International (pp. 4503–4506). http://dx.doi.org/10.1109/IGARSS.2010.5649888.

Marinkovic, P., & Larsen, Y. (2015). *On Resolving the Local Oscillator Drift Induced Phase Ramps in ASAR and ERS1/2 Interferometric Data — The Final Solution, in: Fringe 2015 workshop (ESA SP-731).*

Markowski, P., & Richardson, Y. (Eds.). (2010). *Mesoscale Meteorology in Midlatitudes* (Edition 1). Southern Gate, Ghichester, West Succex, UK: Wiley-Blackwell.

Michalakes, J., Dudhia, J., Gill, D., Henderson, T., Klemp, J., Skamarock, W., & Wang, W. (2004). The weather reseach and forecast model: software architecture and performance. In G. Mozdzynski (Ed.), *Proceedings of the 11th ECMWF Workshop on the Use of High Performance Computing in Meteorology*. Reading: United Kingdom.

Niell, A., Coster, A., Solheim, F., Mendes, V., Toor, P., Langley, R., & Upham, C. (2001). Comparison of measurements of atmospheric wet delay by radiosonde, water vapor radiometer, GPS, and VLBI. *Journal of Atmospheric and Oceanic Technology*, 18, 830–850. http://dx.doi.org/10.1175/1520-0426(2001)018<0830:COMOAW>2.0.CO;2.

Onn, F., & Zebker, H. (2006). Correction for interferometric synthetic aperture radar atmospheric phase artifacts using time series of zenith wet delay observations from a GPS network. *Journal of Geophysical Research*, 111. http://dx.doi.org/10.1029/2005JB004012.

Puysseégur, B., Michel, R., & Avouac, J. (2007). Tropospheric phase delay in interferometric synthetic aperture radar estimated from meteorological model and multispectral imagery. *Journal of Geophysical Research*, 112. http://dx.doi.org/10.1029/2006JB004352.

Rosen, P., Henley, S., Peltzer, G., & Simons, M. (2004). Updated Repeat Orbit Interferometry Package Released. *Eos, Transactions of the American Geophysical Union*, 85, 47-47. http://dx.doi.org/10.1029/2004EO050004.

Saha, S., Moorthi, S., Pan, H.L., Wu, X., Wang, J., Nadiga, S. Goldberg, M. (2010). *NCEP Climate Forecast System Reanalysis (CFSR) 6-hourly Products, January 1979 to December 2010.* http://dx.doi.org/10.5065/D69K487J [Accessed Dec 2013].

Smith, E., & Weintraub, S. (1953). The constants in the equation of atmospheric refractive index at radio frequencies. *Proceedings of the IRE*, 41, 1035–1037. http://dx.doi.org/10.1109/JRPROC.1953.274297.

Unidata, University Corporation for Atmospheric Research and National Centers for Environmental Prediction, National Weather Service, NOAA, U.S. Department of Commerce, & European Centre for Medium-Range Weather Forecasts (2003). *Historical Unidata Internet Data Distribution (IDD) Gridded Model Data, December 2002–current.* URL: http://rda.ucar.edu/datasets/ds335.0/. ([Accessed Dec 2013]).

Wadge, G., Webley, P., James, I., Bingley, R., Dodson, A., Waugh, S. Clarke, P. (2002). Atmospheric models, GPS and InSAR measurements of the tropospheric water vapour field over Mount Etna. *Geophysical Research Letters*, 29. http://dx.doi.org/10.1029/2002GL015159.

Walters, R., Elliott, J., Li, Z., & Parsons, B. (2013). Rapid strain accumulation on the Ashkabad fault (Turkmenistan) from atmosphere-corrected InSAR. *Geophysical Research Letters*, 118, 3674–3690. http://dx.doi.org/10.1002/jgrb.50236.

Walters, R., Parsons, B., & Wright, T. (2014). Constraining crustal velocity fields with InSAR for Eastern Turkey: limits to the block-like behaviour of Eastern Anatolia. *Journal of Geophysical Research*, 119, 5215–5234. http://dx.doi.org/10.1002/2013JB010909.

Walters, R.J., Elliott, J.R., D'Agostino, N., England, P.C., Hunstad, I., Jackson, J.A. Roberts, G. (2009). The 2009 L'Aquila earthquake (central Italy): A source mechanism and implications for seismic hazard. *Geophysical Research Letters*, 36. http://dx.doi.org/10.1029/2009GL039337.

Wessel, P., & Smith, W. (1991). Free Software helps Map and Display Data. *Eos, Transactions of the American Geophysical Union*, 72, 445–446. http://dx.doi.org/10.1029/90EO00319.

Wicks, C., Dzurisin, D., Ingebritsen, S., Thatcher, W., Lu, Z., & Iverson, J. (2002). Magmatic activity beneath the quiescent Three Sisters volcanic center, central Oregon Cascade Range, USA. *Geophysical Research Letters*, 29, 26-1–26-4. http://dx.doi.org/10.1029/2001GL014205.

Williams, S., Bock, Y., & Fang, P. (1998). Integrated satellite interferometry: tropospheric noise, GPS estimates and implications for interferometric synthetic aperture radar products. *Journal of Geophysical Research*, 103, 27051–27067. http://dx.doi.org/10.1029/98JB02794.